

Deep and fast live imaging with two-photon scanned light-sheet microscopy

Thai V Truong^{1,3}, Willy Supatto¹⁻³, David S Koos¹, John M Choi¹ & Scott E Fraser¹

We implemented two-photon scanned light-sheet microscopy, combining nonlinear excitation with orthogonal illumination of light-sheet microscopy, and showed its excellent performance for *in vivo*, cellular-resolution, three-dimensional imaging of large biological samples. Live imaging of fruit fly and zebrafish embryos confirmed that the technique can be used to image up to twice deeper than with one-photon light-sheet microscopy and more than ten times faster than with point-scanning two-photon microscopy without compromising normal biology.

The ability to image tissues or organisms in three dimensions over time (four-dimensional (4D) imaging) has an increasingly important role in modern biology. Fundamental light-matter interactions, such as light scattering, absorption and photodamage (phototoxicity and photobleaching), set the limits of various imaging technologies in terms of spatial resolution, acquisition speed and penetration depth (how deep into a sample useful information can be collected). Often, optimizing any one of these parameters means degrading performance in the others¹. Such tradeoffs are seen in comparing two-photon laser point-scanning microscopy (2P-LSM) and light-sheet microscopy: the former excels at penetration depth in scattering tissues; the latter offers higher acquisition speed and low photodamage. The 2P-LSM (ref. 2) has become the gold standard in deep-tissue microscopic imaging because its point-scanning approach and the use of lower scattering near-infrared light confines the excitation, and its nonimaging detection collects both ballistic and scattered signal photons. The acquisition speed of 2P-LSM is limited because the image is built up one voxel at a time. In contrast, light-sheet microscopy, a century-old technology³ that has been advanced in recent years⁴, illuminates the sample with a plane of visible light, generating one-photon-excited fluorescence from a thin optical section, which is then imaged with a wide-field camera oriented orthogonally to the light sheet. This technique is also known as selective-plane illumination microscopy (SPIM)⁵, and we refer to it as 1P-SPIM. Axial sectioning results from the thinness of the light sheet; lateral resolution is determined by

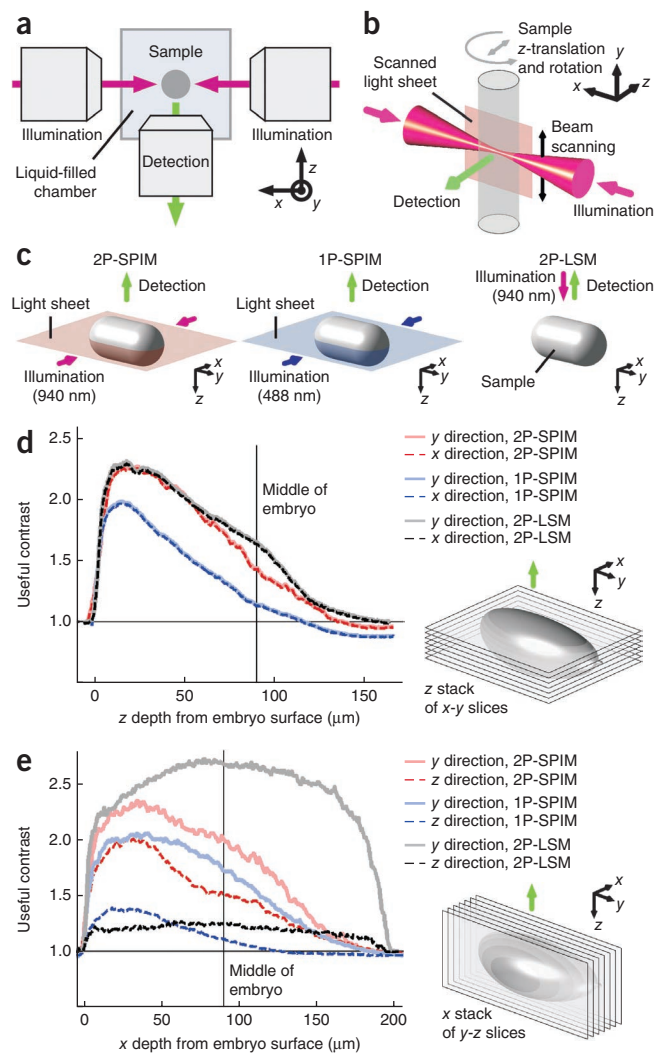
the detection optics (Supplementary Discussion 1). The orthogonal geometry between the illumination and detection pathways, compared to the collinear geometry of conventional microscopy, enables higher imaging speed owing to the parallel image collection and reduces photodamage because only a single focal plane of the sample is illuminated at a time. The penetration depth of SPIM into tissue is limited owing to (i) wide-field detection in which the image from ballistic fluorescence photons is blurred by scattered photons and (ii) thickening of the light sheet by scattering as it traverses the sample, decreasing axial resolution.

To combine the advantages of 2P-LSM and SPIM, we developed two-photon scanned light-sheet microscopy (2P-SPIM). It uses ultrafast near-infrared laser pulses to create a two-photon excitation light sheet, exploiting both nonlinear excitation to achieve high penetration depth and the orthogonal geometry of light-sheet illumination to achieve high acquisition speed and low photodamage. Our 2P-SPIM setup (Fig. 1a,b, Supplementary Fig. 1, Supplementary Video 1 and Supplementary Results 1) is a modification of a 1P-SPIM setup (also termed digital scanned laser light-sheet fluorescence microscopy; DSLM⁶) in which we added (i) a femtosecond-pulsed near-infrared laser and associated optical components to perform 2P- and 1P-SPIM on the same setup; and (ii) bidirectional illumination to increase the useful field of view⁷. In our setup the light sheet is generated along the *x-y* plane, perpendicular to the detection (*z*) axis by laterally scanning the spherically focused laser along the *y* direction⁶ (Fig. 1a,b). This scanned sheet critically yields more than 100-fold higher signal rate (fluorescence signal photons per unit input average laser power) than the cylindrically focused illumination of the static sheet previously used⁸ because of the quadratic dependence of the two-photon-excited fluorescence signal on the excitation intensity (Supplementary Discussion 2). Furthermore, the scanned sheet enables 2P-SPIM to reach similar signal rate as conventional 2P-LSM, even though the illumination numerical aperture is substantially smaller (by a factor of 10 in our case) (Supplementary Fig. 2 and Supplementary Results 2).

The 2P-SPIM should offer better axial resolution than 1P-SPIM at large sample depth by two mechanisms: (i) scattering of excitation light is reduced at near-infrared (compared to visible) wavelengths leading to a better preservation of the light-sheet thickness, and (ii) the quadratic dependence on the excitation light intensity of two-photon-excited fluorescence makes scattered illumination light less important, as fluorophore excitation is spatially confined to only the highest intensity part of the beam, thus preserving axial resolution even when the light sheet is thickened by scattering. These two mechanisms also lead to lower background fluorescence, which improves the apparent

¹California Institute of Technology, Beckman Institute, Pasadena, California, USA. ²Laboratory for Optics and Biosciences, Ecole Polytechnique, Centre National de la Recherche Scientifique, Institut de la Santé et de la Recherche Médicale, Palaiseau, France. ³These authors contributed equally to this work. Correspondence should be addressed to T.V.T. (tvt@caltech.edu) or S.E.F. (sefraser@caltech.edu).

Figure 1 | Optical setup and quantitative analysis of penetration depth. (a,b) Schematic of SPIM: sample is illuminated with near-infrared or visible light (magenta) for 2P- or 1P-excitation, focused with two low-numerical-aperture microscope objective lenses, and the fluorescence signal (green) is detected orthogonally (z direction) by a charge-coupled device (CCD) camera (not shown) through a high-numerical-aperture water-immersion objective lens (a). The illumination light sheet (x-y plane) is generated by laser beam scanning in the y direction (b). (c) Schematic showing the 3D geometry of the illumination and detection light paths for the three imaging modalities compared in this study. (d,e) Quantitative analysis of the z depth (d) and x depth (e) penetration performance of the three imaging modalities. The useful contrasts were calculated for individual image x-y and y-z image slices from 3D datasets similar to those presented in **Figure 2d-f**, averaged over six embryo samples for each imaging modality.



lateral resolution of 2P-SPIM compared to 1P-SPIM. Reduced background should also result from the lower tissue autofluorescence from near-infrared excitation wavelengths.

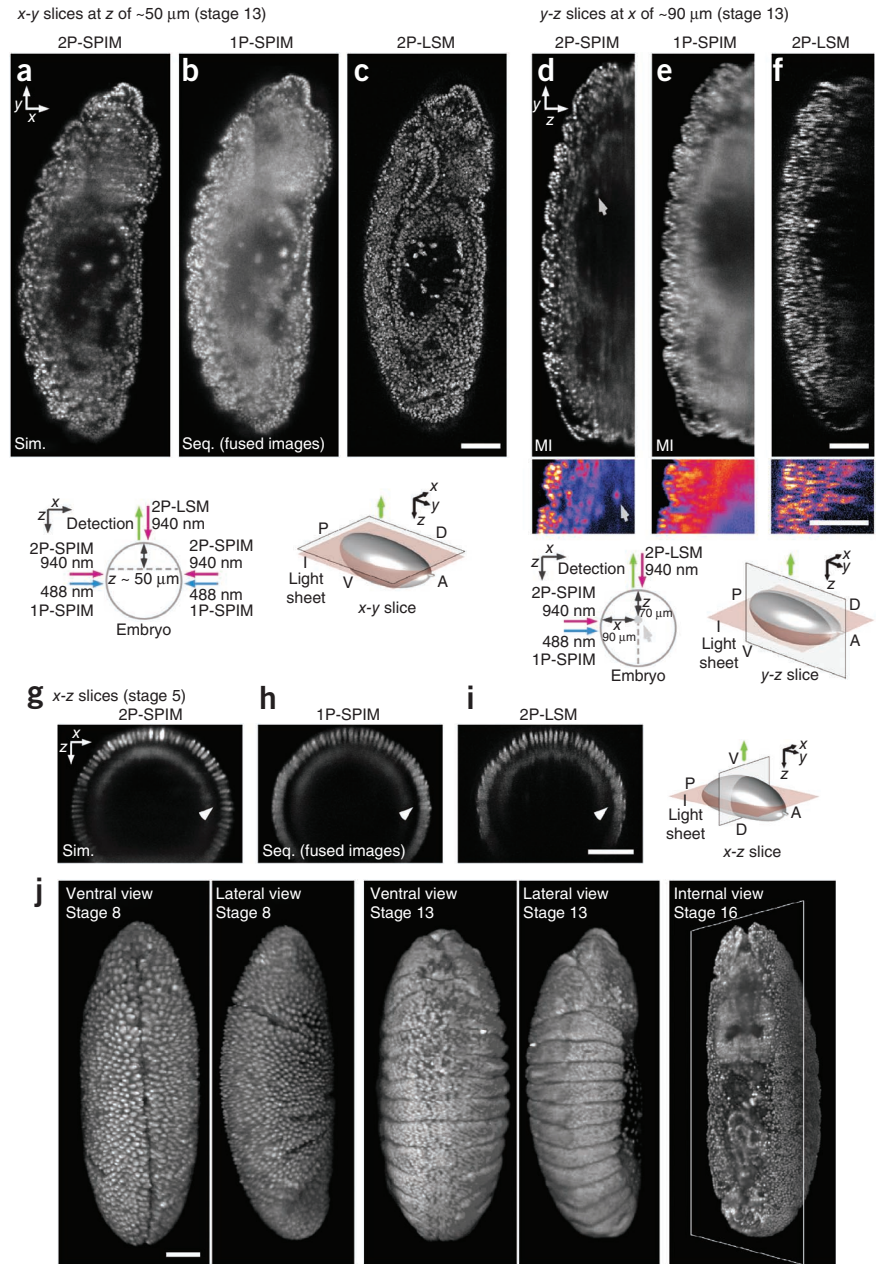
Comparing 2P-SPIM to 2P-LSM, the scattering of the emitted fluorescence on its way to the camera should blur the recorded image in 2P-SPIM and reduce lateral resolution at large sample depths. This drawback is partially offset by the about tenfold lower illumination numerical aperture of 2P-SPIM, which minimizes the resolution-degrading effects from sample-induced inhomogeneities and aberrations (**Supplementary Fig. 3**).

To test the above predictions, we compared the depth performance of 2P-SPIM, 1P-SPIM and 2P-LSM (**Fig. 1c-e**) in three-dimensional (3D) imaging of live fruit fly embryos with GFP-labeled nuclei (**Fig. 2**). The x-y image slices of the 3D datasets demonstrated the lateral resolution achieved deep inside the sample (**Fig. 2a-c**). The background of 2P-SPIM was consistently less than that of 1P-SPIM and consistently more than that of 2P-LSM, resulting in 2P-SPIM achieving better apparent lateral resolution than 1P-SPIM and worse apparent resolution than 2P-LSM, as predicted. The y-z image slices of the 3D datasets illustrate the axial resolution performance (**Fig. 2d-f**) and show that the axial resolution achieved at high sample depth by 2P-SPIM is superior to both 1P-SPIM and 2P-LSM. For 2P-LSM, the imaging depth is simply the distance along the axial (z) direction; in contrast, for SPIM techniques, there are two imaging depths, one along the illumination (x, lateral) direction and one along the detection (z, axial) direction (**Fig. 1c** and **Supplementary Fig. 3**). We collected the y-z image slices shown in **Figure 2d-f** at illumination depth of $x \sim 90 \mu\text{m}$, in the middle of the 3D sample where SPIM imaging is most challenging. As the detection pathway was identical for 2P- and 1P-SPIM, the gain in axial resolution of 2P-SPIM comes directly from the nonlinear excitation. Comparing 2P-SPIM and 2P-LSM (**Fig. 2d,f**) we observed that images of cell nuclei remained relatively undistorted with 2P-SPIM but appeared axially elongated at higher detection depths with 2P-LSM. This elongation comes from strong aberration effects in 2P-LSM that we did not observe with 2P-SPIM owing to its smaller illumination numerical aperture, resulting in more isotropic resolution at large depths for 2P-SPIM. We also imaged early fly embryos (**Fig. 2g-i**, **Supplementary Fig. 4** and **Supplementary Video 2**) and found that 2P-SPIM resolved nuclei around the embryo well past the midpoint of the sample z-dimension depth, whereas 1P-SPIM and 2P-LSM resolved nuclei only to the midpoint.

To quantitatively analyze the performance comparisons described above, we performed spatial frequency analyses of the

3D datasets shown in **Figure 2d-f**. We define a metric called the useful contrast, which measures the contrast only in the range of length scales pertaining to relevant biological structures in the images. The useful contrast then quantifies for each spatial direction the overall quality of the images, taking into account simultaneously the resolution, contrast and signal-to-noise ratio (SNR); any of these alone would not be an adequate metric to compare the images obtained from the three different imaging modalities (**Supplementary Fig. 5** and **Supplementary Results 3**). To quantify the penetration depth in the detection direction, we analyzed the lateral y- and x-direction useful contrasts as functions of the z-dimension depth (**Fig. 1d**). The useful contrast has a value of 1 for a noisy image that has no information content. The analysis showed that lateral useful contrast of 2P-SPIM was higher than that of 1P-SPIM for depths greater than $10 \mu\text{m}$ and was similar to that of 2P-LSM for up to $z \sim 60 \mu\text{m}$. At the center of the embryo ($z \sim 90 \mu\text{m}$), 2P-LSM performed better than 2P-SPIM in terms of lateral useful contrast. To quantify the penetration depth in the illumination direction, we analyzed the axial z-direction useful contrast as a function of the x-dimension depth (**Fig. 1e**). This analysis illustrates the main advantage of 2P-SPIM in maintaining high axial image quality deep in the sample compared to the other techniques: 2P-SPIM performed better in z-direction useful contrast than both 1P-SPIM and 2P-LSM for

Figure 2 | High imaging depth of 2P-SPIM compared with 1P-SPIM and 2P-LSM in 3D imaging of fly embryos with GFP-labeled nuclei. (a–c) *x-y* image slices of stage-13 embryos, obtained using the indicated imaging modalities at $z \sim 50 \mu\text{m}$ from embryo surface. Sim., simultaneous bidirectional illumination; seq., sequential bidirectional illumination. (d–f) *y-z* image slices of stage-13 embryos at $x \sim 90 \mu\text{m}$ from embryo surface (middle of the embryo). MI, monodirectional illumination. Arrows in **d** indicate a deep cell at $x \sim 90 \mu\text{m}$ and $z \sim 70 \mu\text{m}$ (magnified images at bottom with color map enhancing the contrast). In schematics, light red and gray planes denote the light sheet and the computational slice of the 3D dataset, respectively; green arrow denotes the signal detection direction, and magenta and blue arrows denote the illumination directions. A, anterior; P, posterior; D, dorsal; and V, ventral. (g–i) *x-z* image slices of stage-5 embryos. Arrowheads denote the midpoint. (j) Shown are 3D renderings of live fly embryos at various developmental stages imaged with 2P-SPIM, with simultaneous bidirectional illumination. Scale bars, $50 \mu\text{m}$.



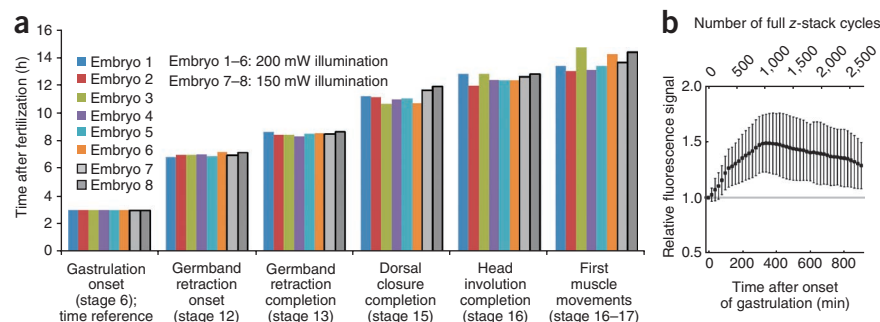
essentially the entire illumination depth. Notably, 1P-SPIM outperformed 2P-LSM in z -direction useful contrast up to $\sim 60 \mu\text{m}$ into the embryo. We collected the 2P- and 1P-SPIM datasets used for this analysis with monodirectional illumination to demonstrate the illumination depth limits; for a realistic imaging application, bidirectional illumination provides complete coverage of the sample (**Supplementary Fig. 6**). Overall, we conclude that for imaging of fly embryos, the penetration depth of 2P-SPIM is about two times better than that of 1P-SPIM and is competitive with that of 2P-LSM (being worse laterally but better axially).

Photodamage propensity is a critical property of any live imaging modality because it fundamentally limits the acquisition speed by limiting the maximum tolerable dosage of excitation light. For imaging with 2P-excitation, previous work has shown that photodamage results from supra-quadratic absorption processes⁹; thus, lower laser peak intensity reduces photodamage. We expected 2P-SPIM, with its much lower peak intensity at a given average laser power used for light-sheet illumination, to induce substantially less photodamage than conventional 2P-LSM (the tenfold smaller illumination numerical aperture yielded a 100-fold smaller peak intensity) (**Supplementary Discussion 3**). To test the low photodamage of 2P-SPIM, we exposed fly embryos to continuous illumination with 200 mW of average excitation power (about 5 times higher than the phototoxicity threshold for these samples when imaged with conventional 2P-LSM¹⁰), enabling fast 4D imaging for up to ~ 18 h from before gastrulation until the end of the embryonic development (**Figs. 2j, 3** and **Supplementary Video 3**). Imaged embryos survived and hatched at the same rate

as control nonilluminated embryos, underwent normal timed sequence of development and showed no phenotypic signs of phototoxicity (**Fig. 3a**, **Supplementary Fig. 7** and **Supplementary Results 4**). In addition, photobleaching of the fluorescence labels was negligible, as no apparent decrease in signal was detected after more than 2,500 cycles of z -dimension stack (z -stack) acquisitions (**Fig. 3b**). These results confirmed the low photodamage propensity of 2P-SPIM compared with 2P-LSM, allowing at least a fivefold increase in tolerable excitation power.

As the signal rates of 2P-SPIM and 2P-LSM were similar, the fivefold increase in excitation power that could be used in 2P-SPIM led to a 25-fold increase in fluorescence (excitation intensity was well below saturation). This increase in signal directly enabled higher acquisition speed and or higher SNR for 2P-SPIM. Combined with multiview imaging^{5,11} in which the sample is rotated by 180° to collect two opposing overlapping z -stacks, the high signal level of 2P-SPIM at 200 mW excitation power allowed

Figure 3 | Non-photodamaging 4D imaging of fly development with 2P-SPIM. **(a)** Analysis of developmental stages of embryos imaged using high laser power. Embryos 1–6 were constantly illuminated with total excitation power of 200 mW, and embryos 7–8 with 150 mW, for ~18 h from pre-gastrulation (stage 4–5) until hatching (stage 17). All embryos were scanned through the light sheet at $10 \mu\text{m s}^{-1}$ over their entire depth ($190 \mu\text{m}$) every 20 s, with z-stack imaging taken at 10 frames s^{-1} . Gastrulation onset served as a time reference (3 h of development) to synchronize the sequences. **(b)** Relative fluorescence signal, summed over the entire z-stacks, averaged over embryos 1–6 and normalized to the signal at the onset of gastrulation (gray line at 1), is plotted as a function of time. Error bars, s.d. for these 6 embryos.



for fast, high-resolution 3D imaging of the entire fly embryo, with high spatial sampling ($400 \text{ voxels} \times 900 \text{ voxels} \times 200 \text{ voxels}$ (x , y and z , respectively) with voxel size of $0.635 \mu\text{m} \times 0.635 \mu\text{m} \times 1 \mu\text{m}$) at 10 frames s^{-1} with time resolution of under 45 s (total volume exposure time was under 25 s) (**Supplementary Fig. 6** and **Supplementary Videos 4–6**). At these imaging conditions, the volume acquisition speed was more than an order of magnitude faster than what is achievable with conventional 2P-LSM before the onset of phototoxicity¹⁰. The 2P-SPIM approach is capable of even faster acquisition speed, beyond video rate: we imaged the beating heart inside a live 5.4-day-old zebrafish embryo using 50 mW total excitation power, achieving cellular resolution at 70 frames s^{-1} (limited by camera readout speed) for a $400 \text{ pixels} \times 400 \text{ pixels}$ field of view ($11.2 \text{ million pixels s}^{-1}$, comparable to rates achieved by 1P-SPIM imaging of similar samples at younger developmental stages¹²), capturing the fast motion of the heart walls and valve leaflets without any sign of phototoxicity (**Supplementary Fig. 8** and **Supplementary Video 7**).

In summary, 2P-SPIM achieves both high imaging depth into biological tissues and high imaging speed without compromising normal biology. Because the improved penetration depth of 2P-SPIM comes entirely from optimizing illumination, approaches that optimize wide-field detection, such as deconvolution¹³ or noncoherent structured illumination¹⁴, could be applied for further improvement. Capabilities of 2P-SPIM could be extended by implementation of recent developments that improve 1P-SPIM or 2P-LSM: multiangle illumination⁷, adaptive optics¹⁵ and focal volume engineering such as the use of Bessel beam illumination^{16,17} (**Supplementary Discussion 4**). The main disadvantages of 2P-SPIM come from the high cost of ultrafast lasers and the fact that multicolor imaging is often less amenable with two-photon compared with one-photon excitation. The intrinsic similar signal rate of 2P-SPIM compared to 2P-LSM, coupled with the ability of 2P-SPIM to accommodate higher excitation power without inducing photodamage, makes 2P-SPIM a fast imaging technique in a fundamental way, more than only because of its parallelized image collection. Thus, in terms of the potential for fast 4D imaging, 2P-SPIM is expected to surpass other parallelized 2P-excitation imaging modalities¹⁸ because these other modalities have lower signal rate (**Supplementary Discussion 4**). Finally, the 2P-SPIM setup can be extended to other nonlinear contrast modalities such as second harmonic generation (SHG)-SPIM, as demonstrated in imaging the label-free SHG signal from collagen fibers in a mouse tail (**Supplementary Fig. 9** and **Supplementary Results 5**). SHG-SPIM appears to be

the technique of choice for high-speed imaging of the multidirectional SHG from synthetic nanopores¹⁹.

METHODS

Methods and any associated references are available in the online version of the paper at <http://www.nature.com/naturemethods/>.

Note: Supplementary information is available on the Nature Methods website.

ACKNOWLEDGMENTS

We thank P. Pantazis, W. Dempsey and L. Trinh for help with zebrafish sample preparations, and E. Beaurepaire for comments on the manuscript. This work was supported by grants to S.E.F. from the Caltech Beckman Institute and US National Institutes of Health (Center for Excellence in Genomic Science grant P50HG004071), and a fellowship to W.S. from the Caltech Biology Division.

AUTHOR CONTRIBUTIONS

T.V.T., W.S. and S.E.F. conceived and designed the project with consultation from D.S.K. and J.M.C.; T.V.T. designed and assembled the instrumentation; J.M.C. provided help with instrument software control. T.V.T. and W.S. imaged flies; T.V.T. imaged zebrafish; T.V.T. and D.S.K. imaged mice; W.S. and T.V.T. performed image reconstruction and analysis, and designed the figures; and T.V.T., W.S. and S.E.F. wrote the paper.

COMPETING FINANCIAL INTERESTS

The authors declare competing financial interests: details accompany the full-text HTML version of the paper at <http://www.nature.com/naturemethods/>.

Published online at <http://www.nature.com/naturemethods/>.

Reprints and permissions information is available online at <http://www.nature.com/reprints/index.html>.

- Vermot, J., Fraser, S.E. & Liebling, M. *HFSP J.* **2**, 143–155 (2008).
- Denk, W., Strickler, J.H. & Webb, W.W. *Science* **248**, 73–76 (1990).
- Siedentopf, H. & Zsigmondy, R. *Annalen Der Physik* **10**, 1–39 (1902).
- Huisken, J. & Stainier, D.Y.R. *Development* **136**, 1963–1975 (2009).
- Huisken, J., Swoger, J., Del Bene, F., Wittbrodt, J. & Stelzer, E.H.K. *Science* **305**, 1007–1009 (2004).
- Keller, P.J., Schmidt, A.D., Wittbrodt, J. & Stelzer, E.H.K. *Science* **322**, 1065–1069 (2008).
- Huisken, J. & Stainier, D.Y.R. *Opt. Lett.* **32**, 2608–2610 (2007).
- Palero, J., Santos, S., Artigas, D. & Loza-Alvarez, P. *Opt. Express* **18**, 8491–8498 (2010).
- Ji, N., Magee, J.C. & Betzig, E. *Nat. Methods* **5**, 197–202 (2008).
- Supatto, W., McMahon, A., Fraser, S.E. & Stathopoulos, A. *Nat. Protoc.* **4**, 1397–1412 (2009).
- Preibisch, S., Saalfeld, S., Schindelin, J. & Tomancak, P. *Nat. Methods* **7**, 418–419 (2010).
- Scherz, P.J., Huisken, J., Sahai-Hernandez, P. & Stainier, D.Y.R. *Development* **135**, 1179–1187 (2008).
- Verveer, P.J. *et al. Nat. Methods* **4**, 311–313 (2007).
- Keller, P.J. *et al. Nat. Methods* **7**, 637–642 (2010).
- Ji, N., Milkie, D.E. & Betzig, E. *Nat. Methods* **7**, 141–147 (2010).
- Fahrbach, F.O., Simon, P. & Rohrbach, A. *Nat. Photonics* **4**, 780–785 (2010).
- Planchon, T.A. *et al. Nat. Methods* **8**, 417–423 (2011).
- Carriles, R. *et al. Rev. Sci. Instrum.* **80**, 081101 (2009).
- Pantazis, P., Maloney, J., Wu, D. & Fraser, S.E. *Proc. Natl. Acad. Sci. USA* **107**, 14535–14540 (2010).

ONLINE METHODS

Optical setups. In the SPIM setup (Fig. 1a,b and Supplementary Fig. 1a), continuous-wave visible laser light at 488 nm (LASOS) and femtosecond-pulsed near-infrared laser light (Chameleon Ultra II, Coherent) were combined into a single collinear beam with a dichroic beamsplitter (Semrock); the beam was subsequently split by a 50/50 broadband beamsplitter (Edmund Optics) to create two opposing beams to illuminate the sample from the left and right side via the two illumination objective lenses (LMPL10XIR, numerical aperture (NA) = 0.25, Olympus). Illumination NA of approximately 0.06 and 0.08 were used for the visible and near-infrared beams, respectively, by under-filling the back focal planes of the illumination lenses. Motorized mechanical shutters allowed control of which laser wavelength and which direction (or both), was used to illuminate the sample. A galvanometer scanner (6215HB, Cambridge Technology) positioned upstream of the beamsplitter allowed fast scanning (1 kHz) of the spherically focused illumination beam along the y direction at the sample, generating a scanned light sheet in the x - y plane. Optical sectioning was achieved by the lateral extent of the focused illumination beam, and its Rayleigh range dictated the useful imaging field of view (Supplementary Discussion 1). The two scanned light sheets coming from opposing sides of the sample were adjusted so that their fields of view overlapped slightly at the center of the sample along the x axis, effectively yielding twice the field of view. The optical signal induced by the light sheet was imaged via the water-immersion detection objective lens (W Plan-Apochromat 20 \times , 1.0 NA, Carl Zeiss) and recorded with an electron-multiplying charge coupled device camera (iXon DU885, Andor). The sample was positionally controlled from the top of the sample chamber with a combination of motorized stages (Sutter Instrument, Physik Instrumente and Newport) that allowed translation in x , y and z directions, and rotation angle θ about the y axis. z -stack imaging was implemented by moving the sample in the z direction across the light sheet. Software based on ScanImage²⁰ (<http://www.neuroptikon.org/projects/display/ephys/scanimage/>) and Micro-Manager²¹ (<http://www.micro-manager.org/>) was used for control of SPIM setup. Conventional 2P-LSM imaging was carried out on a commercial point-scanning microscope (LSM 510 NLO, Carl Zeiss) equipped with a femtosecond-pulsed near-infrared laser. For fair comparison of 2P-SPIM, 1P-SPIM and 2P-LSM in imaging of the fly samples, the imaging setups were initially adjusted^{22,23} to achieve the same resolution of ~ 1 μ m laterally and ~ 2 μ m axially in imaging an ideal sample of fluorescent beads embedded in clear agarose gel (Supplementary Fig. 1b and Supplementary Results 1).

Bidirectional illumination. With 1P-SPIM, the strong background necessitated bidirectional illumination to be carried out sequentially⁷, for which a separate data stack was recorded for each illumination from the left and right of the sample, and these two data stacks were fused computationally afterward. For 2P-SPIM, the nonlinear confinement of the fluorescence to the highest-intensity part of the light sheet and the inherent low background allowed bidirectional illumination to be done simultaneously, minimizing the imaging time for capturing a large 3D sample. Note, however, that for a highly refracting and optically inhomogeneous sample, the initially opposing light sheets coming from opposite sides of the sample could deviate

from their original direction, leading to a loss of axial resolution at the region where they overlap for simultaneous bidirectional illumination. The higher the resolution requirement of an imaging application, the worse this potential problem would be. In our 2P-SPIM imaging, with the system axial resolution of 2 μ m, we observed no degradation of the resolution from simultaneous bidirectional illumination.

Multiview imaging. To image the entire fly embryo with 2P-SPIM, we recorded two opposing z -stacks (at sample angular position of $\theta = 0^\circ$ and $\theta = 180^\circ$) with simultaneous bidirectional illumination. For the same coverage with 1P-SPIM, as bidirectional illumination had to be done sequentially, four z -stacks were needed (with left and right illumination for each of angular position $\theta = 0^\circ$ and $\theta = 180^\circ$). z -stacks were taken by scanning the sample in the z direction at speed of 10 μ m s⁻¹ and setting camera imaging speed at 10 frames s⁻¹, capturing a 120- μ m-thick z -stack within 12 s. For embryo thickness of ~ 180 μ m, two opposing 120- μ m-thick z -stacks provided $\sim 25\%$ data overlap, sufficient for stitching of the z -stacks to form the complete dataset. Rotation of the sample by 180° took 9 s. Thus, to capture the entire embryo, a full 3D imaging cycle of the dual-view simultaneous bidirectional 2P-SPIM (z -stack acquisition, rotation, z -stack acquisition and rotation to initial angular position), plus some overhead time for hardware control, took just under 45 s.

Sample preparation and imaging procedure. All animals were raised and handled according to the guidelines of the California Institute of Technology.

For fly imaging experiments, transgenic *His2Av-GFP65T* fly (*Drosophila melanogaster*) line, with GFP labeling of the cell nuclei, was obtained from the Bloomington Stock Center (#5941). Embryos were collected at 25 $^\circ$ C, staged and dechorionated using standard procedures¹⁰. For SPIM imaging shown in Figure 2 and Supplementary Figures 2,4,5,7 and Supplementary Videos 2–3, heptane glue¹⁰ was used to cement embryos at the surface of a 0.5-mm glass capillary tube (VWR). Embryos were placed with anterior-posterior axis along the length of the capillary and properly oriented so that the side to be imaged from would face away from the capillary, allowing direct optical access to the detection objective lens. The capillary with mounted embryos was then transferred into the water-filled sample chamber for imaging, held from the top with a pipette holder (Warner Instrument). For imaging with 2P-LSM, embryos were mounted as described previously¹⁰. Sample temperature was kept at 22 $^\circ$ C during imaging. All imaged fly embryos were kept for observation after the imaging; they developed normally and hatched within the expected time window. For all comparisons between 2P-SPIM, 1P-SPIM and 2P-LSM, the same embryos were imaged on the same setup for the SPIM techniques, and different but similarly time-staged embryos were imaged with 2P-LSM. The same detection objective lens used in SPIM was used for both illumination and detection in 2P-LSM. For the multiview SPIM imaging (Supplementary Fig. 6 and Supplementary Videos 4–6), the fly embryos were immersed in liquid solution of 1% low-melt agarose at 27 $^\circ$ C and then pulled into a 0.85-mm-diameter glass capillary (VWR) with a stainless steel plunger (VWR). After the agarose solidified at room temperature (21–23 $^\circ$ C) (1–2 min), the capillary was transferred to the sample chamber and the agarose-embedded embryo was extruded from

the capillary to allow full optical access to the sample for imaging. For the long-term imaging photodamage experiments (**Fig. 2j**, **Fig. 3**, **Supplementary Fig. 7** and **Supplementary Video 3**), 10–15 fly embryos at stage 4–5 (before gastrulation) were heptane-glue-mounted on the same capillary. One of the embryos was selected to undergo illumination and imaging, and the rest of the nonilluminated embryos on the same capillary served as controls for the handling and mounting procedure. Embryos were illuminated with two levels of total bidirectional average laser power: 200 mW (6 embryos) and 150 mW (2 embryos) (100 mW and 75 mW, respectively, from each side).

For fast imaging of the zebrafish (*Danio rerio*) beating heart (**Supplementary Fig. 8** and **Supplementary Video 7**), the transgenic line *Tg(flk1-eGFP)*²⁴, with enhanced GFP (eGFP) labeling of the endocardium, was used. The embryos were collected and raised in a low-salt embryo medium (Instant Ocean) per established procedures until the appropriate time for imaging. Phenylthiourea was added to the embryonic raising medium at 20-somite stage to block pigmentation. The embryos were embedded in 1% low-melt agarose (made with 30% Danieau solution) using the same procedure as described above for the fly samples. To prevent movement of the embryos, 0.075% Tricaine was added to both the agarose solution and Danieau solution-filled sample chamber. Sample temperature was kept at 25 °C. To minimize the thermal load associated with imaging at a single focal plane for over 14 s, the excitation wavelength was set at 920 nm, which yielded less water absorption than at the peak absorption of eGFP at ~940 nm. The camera was operated in ‘frame-transfer’ mode, which yielded the maximum frame rate of ~70 frames s⁻¹ for frames of 400 pixels × 400 pixels (0.4 × 0.4 μm pixel⁻¹), with the pixel read-out rate of 35 MHz. The heart rate of the embryo as recorded by the fast imaging was irregular and markedly faster when the embryo was first put into the imaging chamber, likely owing to the trauma of the agarose-embedding procedure. After about 15–30 min, the heart rate decreased and remained at 3.3 Hz, similar to values recorded previously²⁵.

For the SHG-SPIM imaging results shown in **Supplementary Figure 9**, a tip of mouse tail was isolated from a freshly killed mouse (wild type, young adult) following standard procedure, which was then skinned and submerged in fresh 4% paraformaldehyde made in 1× phosphate buffered saline (PBS; pH 7.4). The sample was then fixed at room temperature for 6 h and washed

6 times with PBS. It was then stained in the dark in 75 nM 4'-6-diamidino-2-phenylindole (DAPI) in PBS for 1 h at room temperature and washed repeatedly with PBS until use. For imaging, the tail sample was jammed directly into the opening of a 0.85-mm-diameter glass capillary and immersed in the sample chamber filled with PBS. As the SHG from the collagen fibers in the mouse tail is expected to vary with different linear polarization of the excitation light²⁶, we used circular polarization for excitation and no polarization discrimination for detection to probe the average SHG response of the tissue.

Imaging parameters for all the data presented in our study are presented in **Supplementary Table 1**.

Image processing and analysis. In all figures and videos, basic linear contrast adjustments and maximum intensity projections was performed using ImageJ (US National Institutes of Health) or Imaris (Bitplane) software, except in the following cases. Imaris was used for 3D surface rendering in **Figure 2j**, **Supplementary Figure 7** and **Supplementary Videos 3** and **6**, and for nuclear segmentation in **Supplementary Figure 2c**. For all the 1P-SPIM data that were collected with sequential bidirectional illumination, the data stacks taken with the illumination coming from the +x and -x direction were used to form two half-volumes, separated in the middle of the image x-y plane, and the final presented data (fused images in **Fig. 2b,h** and **Supplementary Fig. 4c,h**) were computationally constructed by simply fusing the two half-volumes. Image stitching and 3D reconstruction in **Supplementary Video 6** (multiview 2P-SPIM imaging) was performed using Imaris. The analysis of the penetration depth using spatial frequency components in Fourier space (**Fig. 1d,e** and **Supplementary Fig. 5**) was performed using Matlab (MathWorks) (**Supplementary Results 3**). Analysis of fast imaging of the zebrafish beating heart (**Supplementary Fig. 8** and **Supplementary Video 7**) was performed using ImageJ and Matlab.

20. Pologruto, T., Sabatini, B. & Svoboda, K. *Biomed. Eng. Online* **2**, 13 (2003).
21. Edelstein, A., Amodaj, N., Hoover, K., Vale, R. & Stuurman, N. *Curr. Protoc. Mol. Biol.* **92**, 14.20.1–14.20.17 (2010).
22. Engelbrecht, C.J. & Stelzer, E.H.K. *Opt. Lett.* **31**, 1477–1479 (2006).
23. Zipfel, W.R., Williams, R.M. & Webb, W.W. *Nat. Biotechnol.* **21**, 1369–1377 (2003).
24. Beis, D. et al. *Development* **132**, 4193–4204 (2005).
25. Kopp, R., Schwerte, T. & Pelster, B. *J. Exp. Biol.* **208**, 2123–2134 (2005).
26. Williams, R.M., Zipfel, W.R. & Webb, W.W. *Biophys. J.* **88**, 1377–1386 (2005).